[Journal of Geophysical Research: Solid Earth]

Supporting Information for

[Non-Volcanic Earthquake Swarm Near the Harrat Lunayyir Volcanic Field, Saudi Arabia]

[M. Youssof, P. M. Mai, A. Nobile, and S. Jónsson]

[King Abdullah University of Science and Technology (KAUST), Thuwal 23955-6900, Saudi Arabia]

Contents of this file

Introduction

The supporting information contains some details for different sections of the main article. This section mainly documents some technical notes about 1) M_L formulas, 2) sensitivity analysis by backprojecting the Incident rays, 3) stress drop estimations, and 4) frequency index analysis.

Text S1. Appendix (A): M_L Formulas

The network-based standard magnitudes produced by the SGS are based on two definitions for M_L formulas (Soliman et al. 2019), depending on the area distances and tectonics. One equation is Eq. (1) of Alsaker et al. (1991), which can only be used for the shield structure and local distances, with epicentral distances $\leq$ 200 km, while Eq. (2) of Bormann (2012), which is recommended for crustal earthquakes within a regional scale (i.e. 200 km $\leq D \leq$ 700 km).

$$M_L \simeq logA_{Smax} + 1.11logR + 0.00189R - 2.09 \quad (1)$$

$$M_L \simeq 0.925logA_{Smax} + 0.91logR + 0.00087R - 1.31 \quad (2)$$

where A_{Smax} is the maximum of the ground velocity absolute amplitude of highpass corner frequency 2Hz, for the S-wave ground velocity (measured in μm/s). R is a distance from the hypocenter to the station in km. Eq. (1) defines the local magnitude scale for the whole region of Lunayyir, thus, we are able to compare the MFDs of any seismic activities within our area of interest as shown in Figure (2).

Text S2. Appendix (B): Sensitivity Analysis by Backprojecting the Incident Rays

The arrival time delays required to bring the signals into phase is a direct estimate of the back azimuth and the slowness of the seismic signals. The total energy (defined by the power spectral density– PSD) recorded at the array can be calculated by the integration of the squared summed amplitudes over time.

The fk diagram (Figure 4c) shows the array response of a selection of our dense-aperture southeastern array (Map of Figure 4b).

For comparison, we calculate the expected phase travel times and ray parameters given the known stations and relocated source coordinates for the same event, using the velocity model we applied in the relocation. As listed in Table S2, the average theoretical values for the ray parameters are 16.1, and 28.7 s/° for P- and S-wave, respectively. These predicted values agree well with the fk-analysis, confirming the observed and relocated hypocenter of the event of interest.

The uncertainty is reasonable between the synthetics and fk results. The difference in slowness values is minimal (0.45 s/°), where the backazimuth values have about 2° difference. A source of such difference is attributed to using one pair of event-station for the synthetics while using several stations in the fk measurements, beside the lack of an accurate 3D velocity model contributes to such difference.

Text S3. Appendix (C): Stress Drop Estimation

We calculate stress drop ($\Delta\sigma$) using the Eshelby (1957) relationship:

$$\Delta\sigma = (\frac{7}{16}) \times (\frac{M_0}{r^3}) \tag{3}$$

in which M_0 is the seismic moment (in N.m), and r is the source radius (in meters). Note that M_0 and M_W values depends on the seismic wave types used in the analysis. Despite using models for both P- and S-phases here, we computed the mean values which further used to estimate ($\overline{\Delta\sigma}$).

To measure the source radius, we use the circular source model of Madariaga (1976) and Brune (1970)

$$r = \frac{\kappa\beta}{f_c} \tag{4}$$

in which we assume β, the shear-wave velocity as 3.4 km/s (based on our velocity model and avergae source depth). While κ depends on the spectra of P and S waves and on the choice of source model.

To estimate the model parameters, we use a standard grid-search method. Previous studies suggested that estimation of source parameters is robust using this technique (e.g., Tusa et al., 2006a, 2006b; Edwards et al., 2008; de Lorenzo et al., 2010). Here, we implement a grid-search over ω_0, and f_c, fixing κ=0.3. To optimize the search process, we adopt a two-level procedure (e.g., Lomax et al. 2000). In the first step, the entire relevant model parameter space is subdivided into a coarse grid. The range of model parameter values in the coarse grid is based on a priori analysis of the dataset (assigning realistic values from the earlier studies on source characterization). At each point of this grid, the observed and the theoretical spectrum are matched using a misfit function of mean absolute error (MAE) performance, which helps to measure accuracy for this continuum of variables. In the second step, a refined grid is built around the initial best estimations, and MAE function is recalculated at each point of this grid to resolve the best-fitting parameters.

Text S4. Appendix (D): Frequency Index Analysis

Buurman and West (2010) developed a measure to discriminate between different types of seismic events, defines the frequency index (FI) based on the ratio of energy in low and high frequency windows:

$$FI = log\left(\frac{\overline{A(hf)}}{\overline{A(lf)}}\right) \tag{5}$$

where ($\overline{A(hf)}$) and ($\overline{A(lf)}$) are, respectively, the average spectral amplitudes across selected bands of high and low range of frequencies.

Because the resulting measure spans many orders of magnitude, we use a base-ten logarithm to reduce the index to a simple number.

To calculate the *FI* in a consistent manner, we first pick the P- and S-onsets, minimizing the time window to approximately the P-S duration, followed by removing the average amplitude from the selected waveforms signals, with a fixed time series duration of 40 seconds: 10 second prior to the earthquake P-onset and 30 seconds after, ensuring that the high frequency signal is fully captured in the Fourier analysis. This is a sufficient time window over which to sample both the shorter duration, smaller magnitude earthquakes recorded, as well as the more emergent, lower frequency events. Linear trends and offsets are removed from the waveforms, and they are transformed to the frequency domain using a tapered Fourier transform.

To avoid problems with noise contamination, only earthquakes with high SNR $\geq$ 3.0 were included. The average noise amplitude was measured and a noise window was chosen such that it ended 15 s before the P-first arrival pick. After calculating the SNR using the amplitudes measured in the earthquake and noise windows, the amplitude of the noise window was subtracted from the earthquake window amplitude.

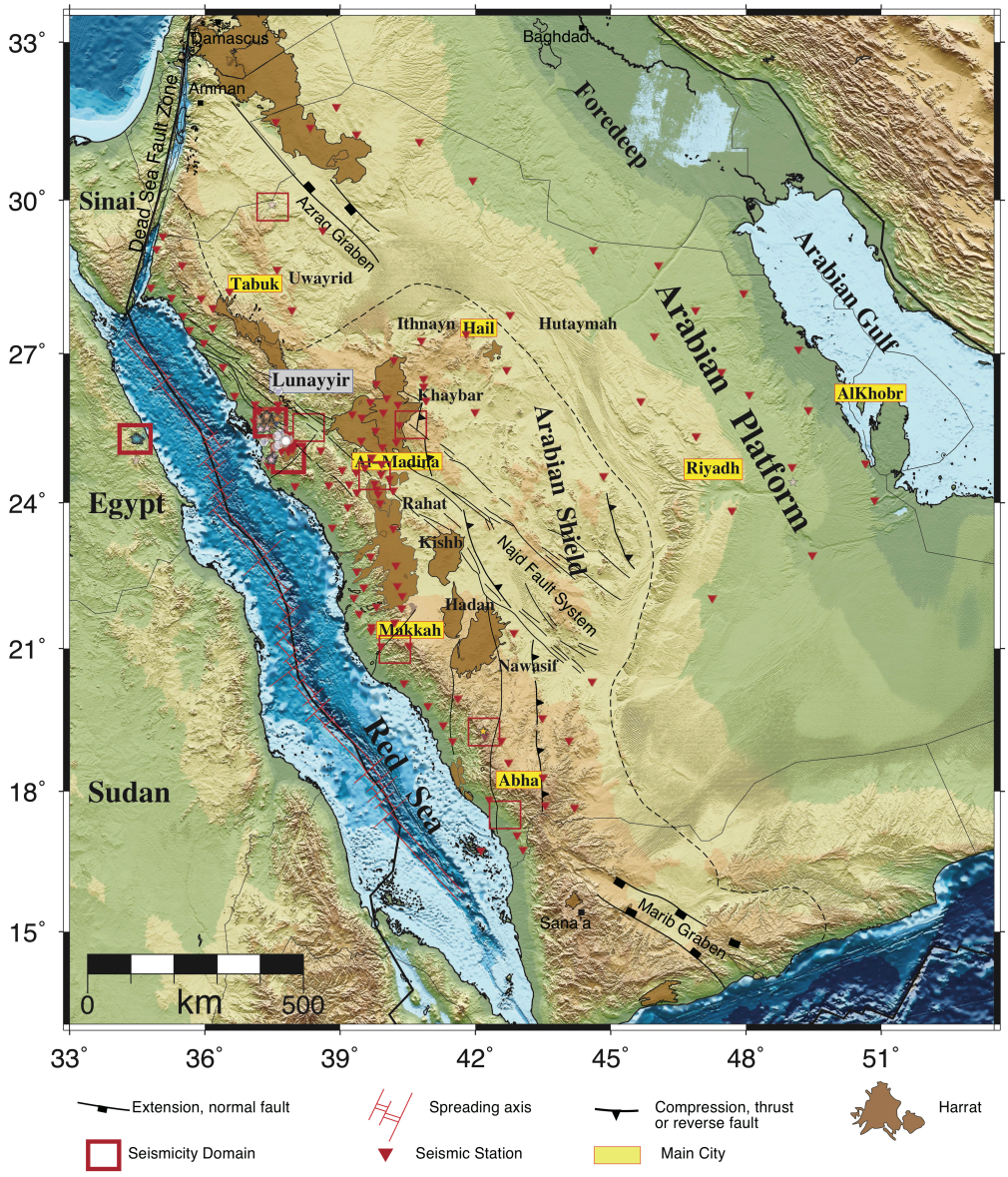

Figure S1: Regional map of Arabia. Volcanic fields (harrats) are shown in brown color. Permanent stations are shown in red color. The places of long- and short-term swarms discussed in the text are highlighted in bold and light red boxes, respectively.

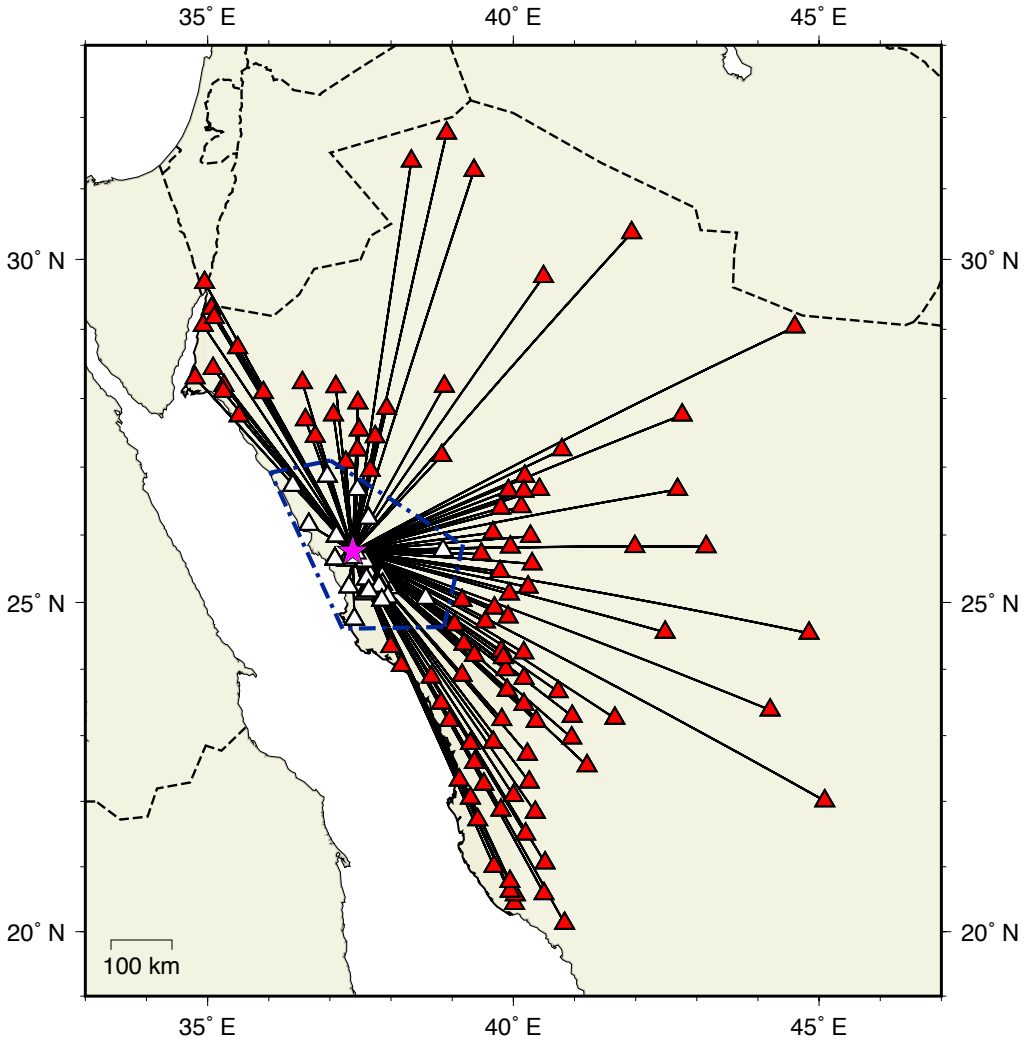

Figure S2: All stations (color-coded with both red and dark yellow colors) used in the first trial to assemble as much records as we can for the first inversion run before selecting the optimum records (from stations in dark yellow) which involved in the final solution.

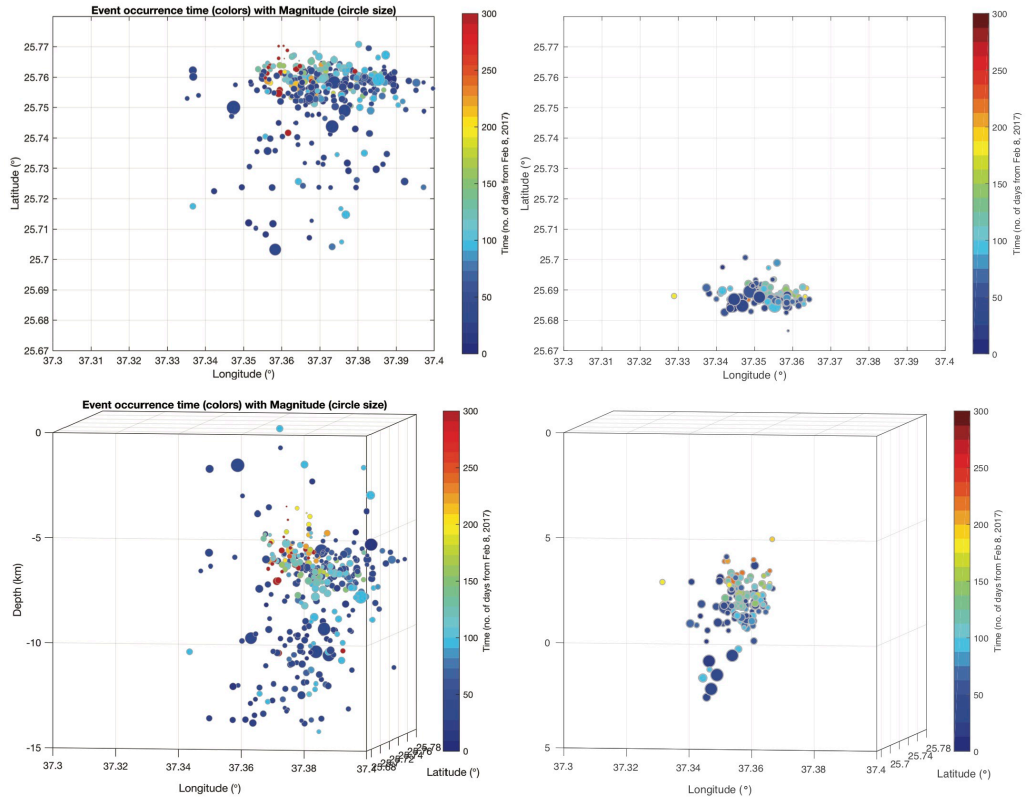

Figure S3: Plan views and vertical cross sections for double-difference relative relocation results using differential traveltimes of both P- and S-phases. The circle size represents the magnitude. An upward migration is clearly observed.

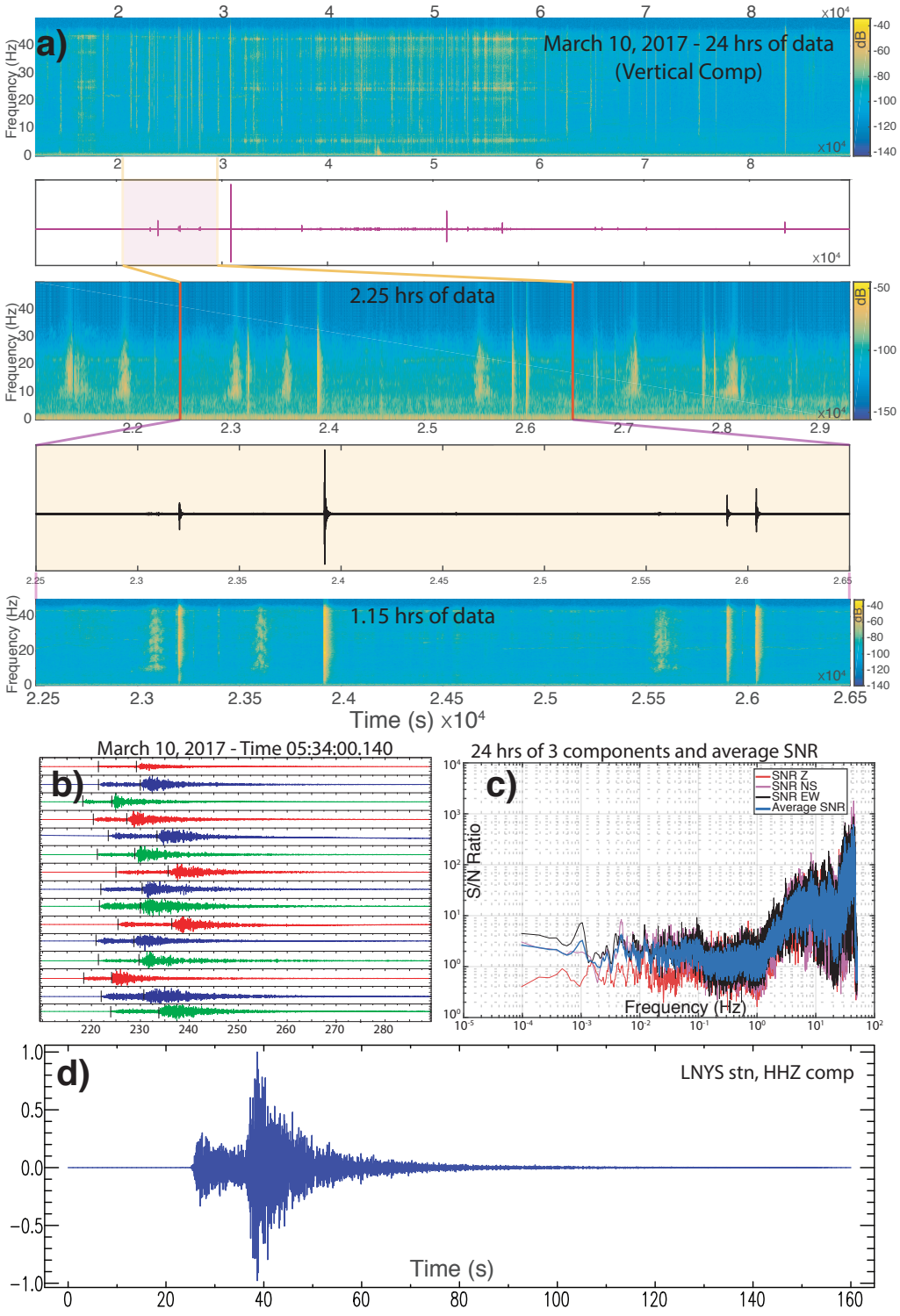

Figure S4: a) Example of data plotted as time-series and frequency domain, helping to identify event-based waveforms, b) Raw seismic data at 15 stations (vertical component), of the largest event with M_W 3.6. The picks of P- and S- phases, used as input for the double-difference analysis. c) SNR example for 24 hours of continuous data at one station. d) One trace out of c) showing a high-quality signal.

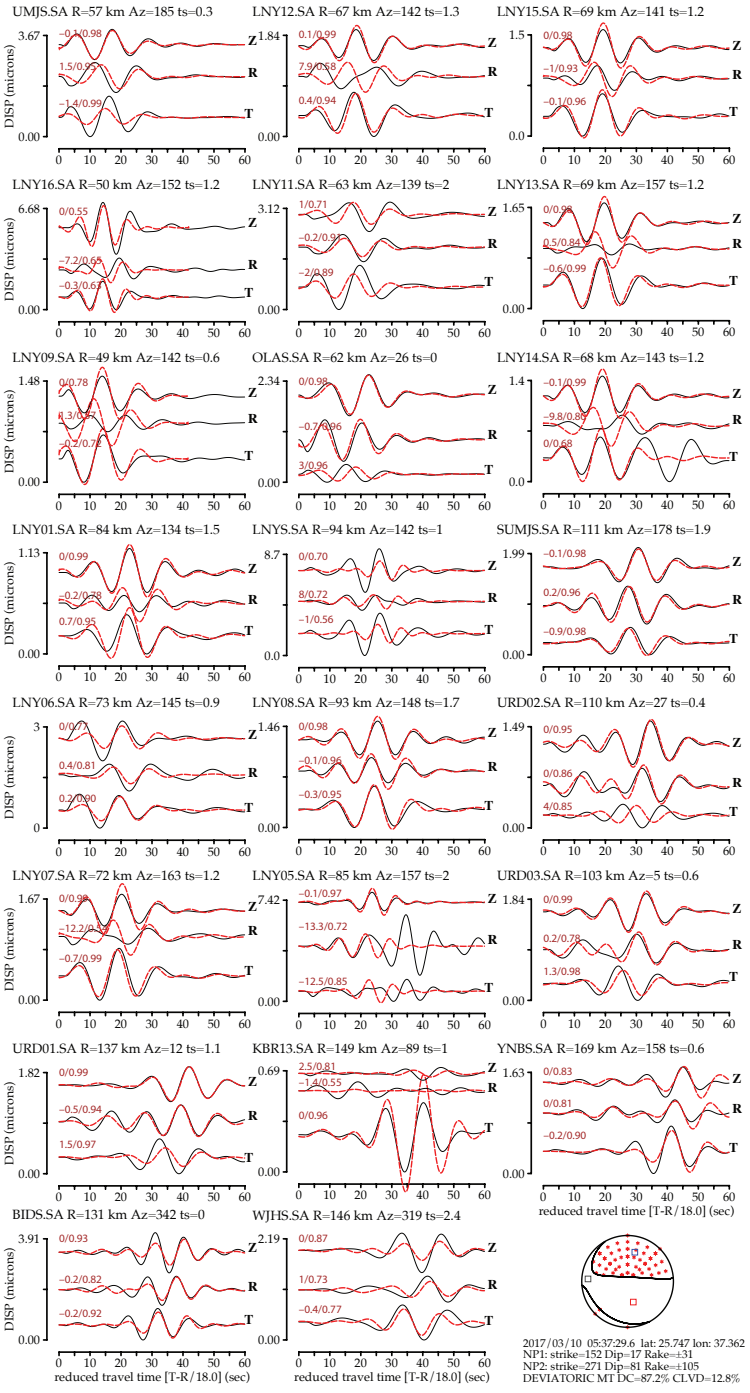

Figure S5: Moment tensor solution for the largest event (March 10th, 2017 at 17:37:10, Umm-Lujj), with waveform fits for the low-frequency data 5-25 s (0.04 Hz – 0.2 Hz)), (red synthetic; black observed displacement data).

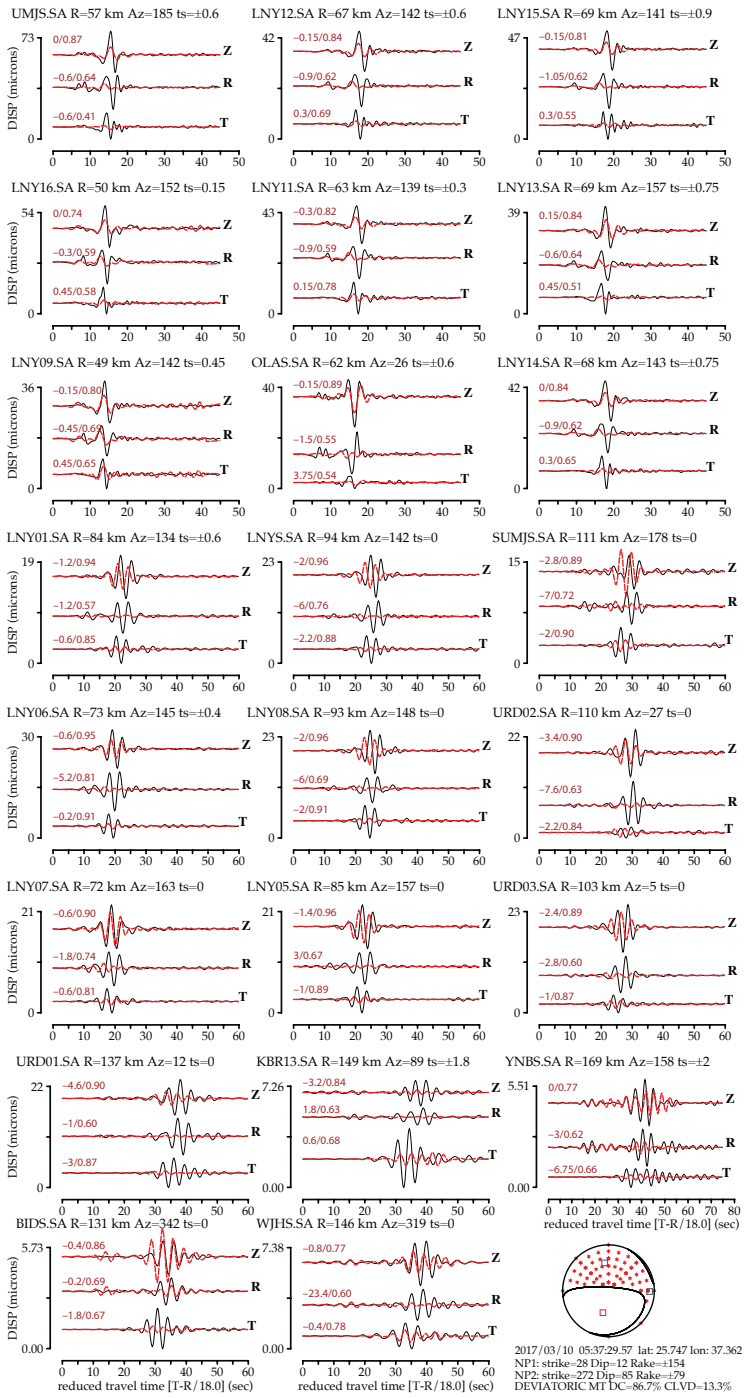

Figure S6: Moment tensor solutions for the largest event (March 10th, 2017 at 17:37:10, Umm-Lujj),with waveform fits for the high-frequency data 1-10 s (0.1 Hz – 1 Hz), (red synthetic; black observed displacement data).

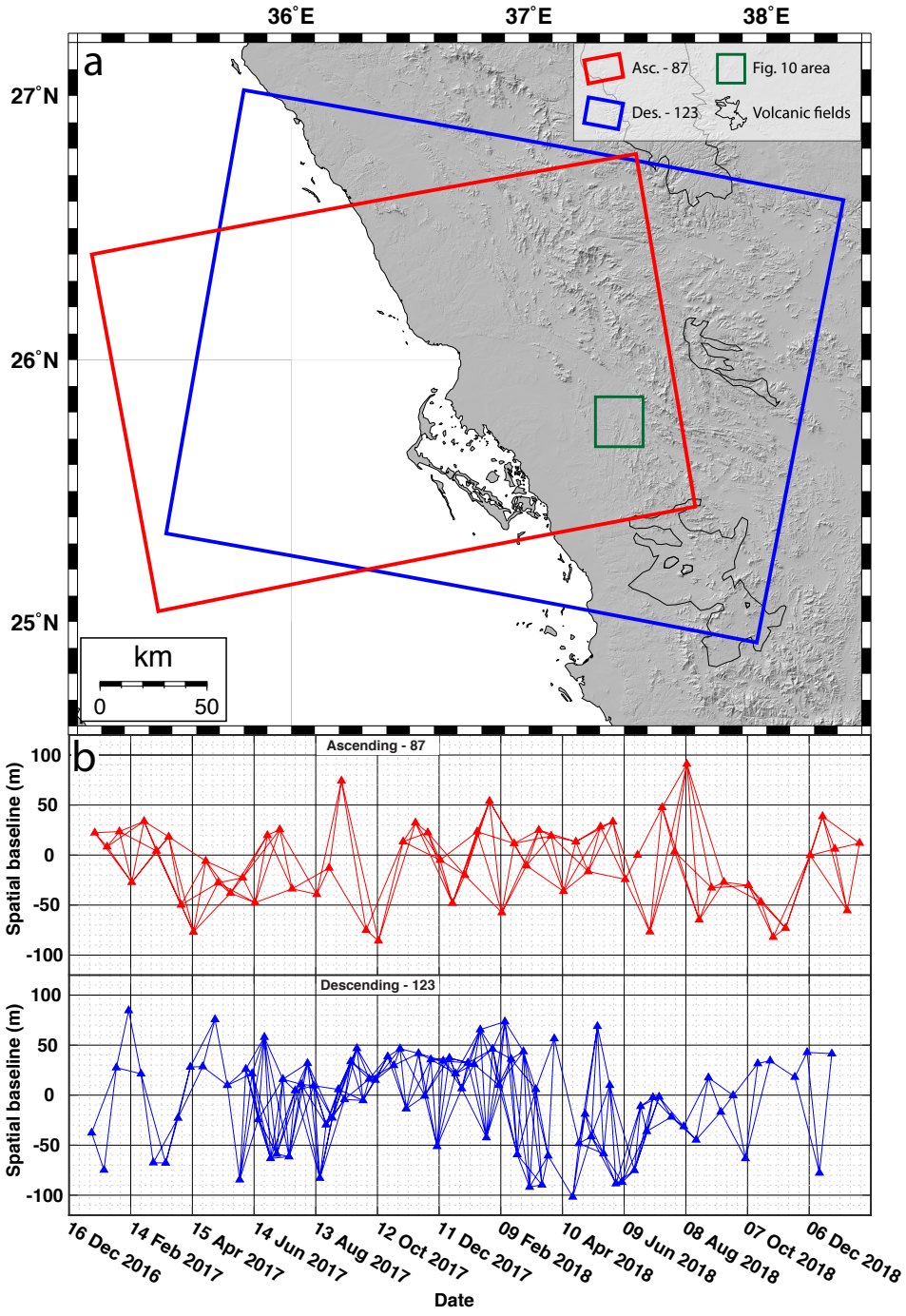

Figure S7: a) The area of interest (green square) is located to the north of Harrat Lunayyir and is covered by two SAR frames in both ascending (red box) and descending (blue box) orbits. b) the interferogram networks used to evaluate the deformation rate maps in figure 10.

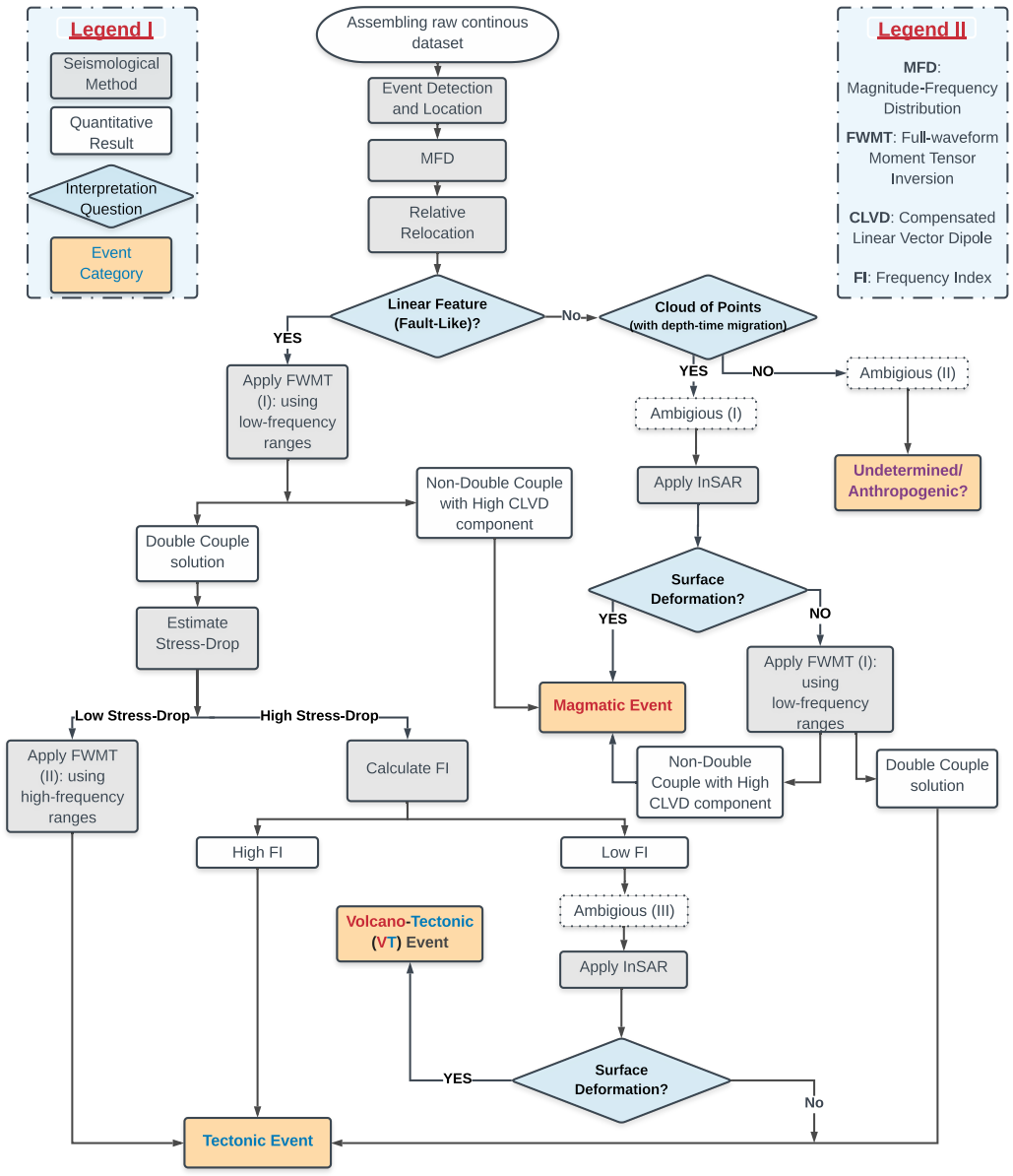

Figure S8: Proposed flow-chart of data processing to implement for distinguishing events nature in such cases of seismic swarm activities.

Table S1: Seismic activity around the Red Sea

Location	**Max. Mag. / Time**	**Duration**
[1]Tabuk eq., North of KSA	M_L 5.1 July 27, 2004	3 months (June - August 2004)
[2]Al-Ays Swarm, North of KSA	M_L 4.2 Nov. 11, 2007	7 months (Oct. 2007 - May 2008)
[3]Badr eq., North of KSA	M_b 4.0 August 23, 2009	1 month (August - Sept. 2009)
[4]Jizan Swarm, South of KSA	M_L 4.5 Jan. 23, 2014	11 months (Jan. - Dec. 2014)
[5]Al-Namas Swarm, North of KSA	M_L 4.1 Nov. 03, 2017	3 months (Nov. 2017 - Jan. 2018)
[6]Abu-Dabab Swarm, South of Egypt	M_L 5.1 July 02, 2004	continuous for decades

[1]Al-Damegh et al. (2009). [2]Mukhopadhyay et al. (2012), Saibi et al. (2019). [3]Aldamegh et al. (2012). [4,5]Abdelfattah et al. (2017, 2020). [6]Badawy et al. (2008).

Table S2: Theoretical travel times and ray parameters of corresponding seismic phases computed using 1-D velocity model

Dist. (°)	**Phase**	**TT (s)**	**Ray Param. (s/°)**	**Inc. (°)**
LNY09				
0.44	P	8.65	18.597	75.94
	S	14.94	32.103	75.95
LNY11				
0.57	P	11.86	17.05	62.81
	S	20.47	29.56	63.28
LNY12				
0.6	P	12.46	17.04	62.79
	S	21.52	29.53	63.23
LNY14				
0.61	P	12.65	17.03	62.77
	S	21.85	29.51	63.21
LNY13				
0.62	P	12.84	17.02	62.75
	S	22.17	29.5	63.2
LNY15				
0.62	P	12.85	17.01	62.75
	S	22.19	29.5	63.2
LNY07				
0.64	P	14.95	13.75	45.84
	S	22.78	29.35	63.17
LNYS				
0.85	P	17.74	13.73	45.78
	S	30.86	24.74	48.38
SUMJS				
0.99	P	19.76	13.68	45.72
	S	34.5	24.5	48.33
Average				
0.66	P	13.75	16.10	58.57
	S	23.48	28.70	61.33

Table S3: Azimuthal dependency of source parameters for the largest event recorded by 68 stations

Azimuth	**Mean/Median**	**Distance**	**SD**	**Moment**	**Mw**	**fc**
All clusters	Median	202.583	5.116	6.308E+13	3.122	2.6
	Mean	192.059	5.491	6.668E+13	3.466	2.8
NE cluster	Median	242.403	5.745	6.073E+13	3.156	2.3
	Mean	232.359	6.995	8.149E+13	3.198	2.6
NW cluster	Median	315.967	4.898	6.544E+13	2.677	3.2
	Mean	305.338	4.920	6.313E+13	4.405	3.1
SE cluster	Median	162.764	4.457	4.803E+13	3.088	2.4
	Mean	173.124	4.714	5.443E+13	3.075	2.7
SW cluster	Single Stn.	57.416	5.334	6.767E+13	3.187	2.8

Table S4: Frequency Index parameters for the stations shown in Figure 9

Event	Station	SNR	*FI*
2009 event	LNYS	86.52	-0.41
	UMJS	81.47	-0.64
2017 event	LNYS	92.93	0.26
	UMJS	94.32	0.18
2018 event	LNYS	92.46	0.37
	UMJ05	86.41	0.025
	UMJ12	89.89	0.011